

## The XMM-Newton optical/UV monitor telescope

K. O. Mason<sup>1</sup>, A. Breeveld<sup>1</sup>, R. Much<sup>2</sup>, M. Carter<sup>1</sup>, F. A. Cordova<sup>3</sup>, M. S. Cropper<sup>1</sup>, J. Fordham<sup>4</sup>, H. Huckle<sup>1</sup>, C. Ho<sup>6</sup>, H. Kawakami<sup>1</sup>, J. Kennea<sup>3</sup>, T. Kennedy<sup>1</sup>, J. Mittaz<sup>1</sup>, D. Pandel<sup>3</sup>, W. C. Priedhorsky<sup>6</sup>, T. Sasseen<sup>3</sup>, R. Shirey<sup>3</sup>, P. Smith<sup>1</sup>, and J.-M. Vreux<sup>5</sup>

<sup>1</sup> Mullard Space Science Laboratory, University College London, Holmbury St. Mary, Dorking, Surrey, RH5 6NT, UK

<sup>2</sup> Astrophysics Division, Space Science Department of ESA, PO Box 299, 2200 AG Noordwijk, The Netherlands

<sup>3</sup> Department of Physics, University of California, Santa Barbara, California 93106, USA

<sup>4</sup> Department of Physics and Astronomy, University College London, Gower Street, London, UK

<sup>5</sup> Institut d'Astrophysique et de Géophysique, Université de Liège, 5 avenue de Cointe, 4000-Liège, Belgium

<sup>6</sup> Los Alamos National Laboratory, PO Box 1663, Los Alamos, NM 87545, USA

Received 2 October 2000 / Accepted 20 October 2000

**Abstract.** The XMM-OM instrument extends the spectral coverage of the *XMM-Newton* observatory into the ultraviolet and optical range. It provides imaging and time-resolved data on targets simultaneously with observations in the EPIC and RGS. It also has the ability to track stars in its field of view, thus providing an improved post-facto aspect solution for the spacecraft. An overview of the XMM-OM and its operation is given, together with current information on the performance of the instrument.

**Key words.** space vehicles: instruments – instrumentation: detectors – ultraviolet: general

### 1. Introduction

The Optical/UV Monitor Telescope (XMM-OM) is a standalone instrument that is mounted on the mirror support platform of *XMM-Newton* (Jansen et al. 2001) alongside the X-ray mirror modules. It provides coverage between 170 nm and 650 nm of the central 17 arcmin square region of the X-ray field of view (FOV), permitting routine multiwavelength observations of XMM targets simultaneously in the X-ray and ultraviolet/optical bands. Because of the low sky background in space, XMM-OM is able to achieve impressive imaging sensitivity compared to a similar instrument on the ground, and can detect a  $B = 23.5$  mag A-type star in a 1000 s integration in “white” light (6 sigma). It is equipped with a set of broadband filters for colour discrimination. The instrument also has gratings for low-resolution spectroscopy, and an image expander (Magnifier) for improved spatial resolution of sources. Fast timing data can be obtained on sources of interest simultaneously with image data over a larger field.

In the following sections we give an overview of the instrument followed by an account of its operation in orbit and the instrument characteristics.

Send offprint requests to: K. O. Mason,  
 e-mail: kom@mssl.ucl.ac.uk

### 2. Instrument overview

The XMM-OM consists of a Telescope Module and a separate Digital Electronics Module, of which there are two identical units for redundancy (see Fig. 1). The Telescope Module contains the telescope optics and detectors, the detector processing electronics and power supply. There are two distinct detector chains, again for redundancy. The Digital Electronics Module houses the Instrument Control Unit, which handles communications with the spacecraft and commanding of the instrument, and the Data Processing Unit, which pre-processes the data from the instrument before it is telemetered to the ground.

#### 2.1. Optics

The XMM-OM uses a Ritchey Chrétien telescope design modified by field flattening optics built into the detector window. The  $f/2$  primary mirror has a 0.3 m diameter and feeds a hyperboloid secondary which modifies the  $f$ -ratio to 12.7. A 45° flat mirror located behind the primary can be rotated to address one of the two redundant detector chains. In each chain there is a filter wheel and detector system. The filter wheel has 11 apertures, one of which is blanked off to serve as a shutter, preventing light from reaching the detector. Another seven filter locations house lenticular filters, six of which constitute a

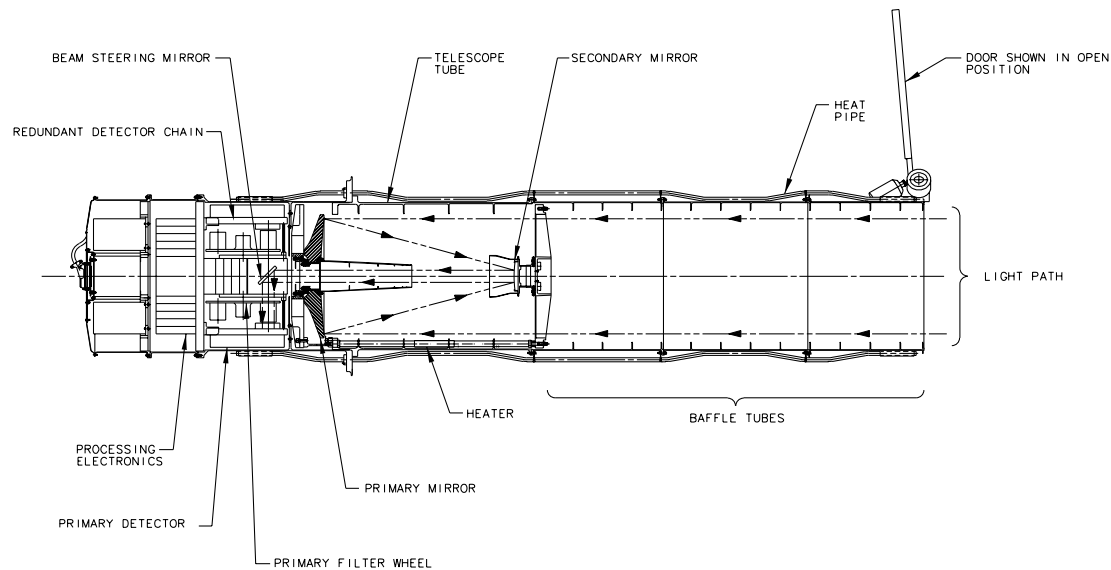


**Fig. 1.** A mechanical drawing of the XMM-OM telescope module showing the light path through to the detectors

set of broad band filters for colour discrimination in the UV and optical between 180 nm and 580 nm (see Table 2 for a list of filters and their wavelength bands). The seventh is a “white light” filter which transmits light over the full range of the detector to give maximum sensitivity to point sources. The remaining filter positions contain two gratings, one optimised for the UV and the other for the optical range, and a  $\times 4$  field expander (or Magnifier) to provide high spatial resolution in a 380–650 nm band of the central portion of the (FOV).

## 2.2. Detector

The detector is a microchannelplate-intensified CCD (Fordham et al. 1992). Incoming photons are converted into photoelectrons in an S20 photocathode deposited on the inside of the detector window. The photoelectrons are proximity focussed onto a microchannelplate stack, which amplifies the signal by a factor of a million, before the resulting electrons are converted back into photons by a P46 phosphor screen. Light from the phosphor screen is passed through a fibre taper which compensates for the difference in physical size between the microchannelplate stack and the fast-scan CCD used to detect the photons. The resulting photon splash on the CCD covers several neighbouring CCD pixels (with a FWHM of approximately 1.1 CCD pixels, if fitted with a Gaussian). The splash is centroided, using a  $3 \times 3$  CCD pixel subarray to yield the position of the incoming photon to a fraction of a CCD pixel (Kawakami et al. 1994). An active area of  $256 \times 256$  CCD pixels is used, and incoming photon events are centroided to 1/8th of a CCD pixel to yield  $2048 \times 2048$  pixels on the sky, each 0.4765 arcsec square. In this paper, to avoid confusion, while CCD pixels ( $256 \times 256$  in FOV) will be referred to explicitly, a pixel refers to a centroided pixel ( $2048 \times 2048$  in FOV). As described later,

images are normally taken with pixels binned  $2 \times 2$  or at full sampling.

The CCD is read out rapidly (every 11 ms if the full CCD format is being used) to maximise the coincidence threshold (see Sect. 5.2).

## 2.3. Telescope mechanical configuration

The XMM-OM telescope module consists of a stray light baffle and a primary and secondary mirror assembly, followed by the detector module, detector processing electronics and telescope module power supply unit. The separation of the primary and secondary mirrors is critical to achieving the image quality of the telescope. The separation is maintained to a level of  $2 \mu\text{m}$  by invar support rods that connect the secondary spider to the primary mirror mount. Heat generated by the detector electronics is transferred to the baffle by heat pipes spaced azimuthally around the telescope, and radiated into space. In this way the telescope module is maintained in an isothermal condition, at a similar temperature to the mirror support platform. This minimizes changes in the primary/secondary mirror separation due to thermal stresses in the invar rods. Fine focussing of the telescope is achieved through two sets of commandable heaters. One set of heaters is mounted on the invar support rods. When these heaters are activated, they cause the rods to expand, separating the primary and secondary mirrors. A second set of heaters on the secondary mirror support brings the secondary mirror closer to the primary when activated. The total range of fine focus adjustment available is  $\pm 10 \mu\text{m}$ .

The filter wheel is powered by stepper motor, which drives the wheel in one direction only. The filters are arranged taking into account the need to distribute the more massive elements (grisms, Magnifier) uniformly across the wheel.

## 2.4. Digital Electronics Module

There are two identical Digital Electronics Modules (DEM) serving respectively the two redundant detector chains. These units are mounted on the mirror support platform, separate from the telescope module. Each DEM contains an Instrument Control Unit (ICU) and a Digital Processing Unit (DPU). The ICU commands the XMM-OM and handles communications between the XMM-OM and the spacecraft.

The DPU is an image processing computer that digests the raw data from the instrument and applies a non-destructive compression algorithm before the data are telemetered to the ground via the ICU. The DPU supports two main science data collection modes, which can be used simultaneously. In Fast Mode, data from a small region of the detector are assembled into time bins. In Image Mode, data from a large region are extracted to create an image. These modes are described in more detail in the next sect. The DPU autonomously selects up to 10 guide stars from the full XMM-OM image and monitors their position in detector coordinates at intervals that are typically set in the range 10–20 s, referred to as a tracking frame. These data provide a record of the drift of the spacecraft during the observation accurate to  $\sim 0.1$  arcsec. The drift data are used within the DPU to correct Image Mode data for spacecraft drift (see Sect. 5.5).

## 3. Observing with XMM-OM

### 3.1. Specifying windows

The full FOV of XMM-OM is a square  $17 \times 17$  arcmin, covering the central portion of the X-ray FOV. Within this field the observer can define a number of data collection windows around targets or fields of interest. Up to five different Science Windows can be defined with the restriction that their boundaries may not overlap. However, one window can be completely contained within another.

Because of constraints on the telemetry rate available, it is not possible to transmit the full data on every photon that XMM-OM detects. Instead a choice has to be made between image coverage and time resolution. Thus two types of Science Window can be defined, referred to as Image Mode and Fast Mode. A maximum of two of the five available science windows can be Fast Mode.

*Image Mode* emphasizes spatial coverage at the expense of timing information. Images can be taken at the full sampling of the instrument or binned by a factor of 2 or 4, to yield a resolution element on the sky of approximately 0.5, 1.0 or 2.0 arcsec (a factor of four finer for the Magnifier). The maximum total size of the Science Windows is determined by the memory available in the DPU. A single Image Mode window binned by a factor of  $2 \times 2$  can be up to  $976 \times 960$  detector pixels, which results in a  $488 \times 480$  binned pixel image being stored in the DPU. At full sampling (with no binning) the window can be up to  $652 \times 652$  pixels. Any drift in the pointing

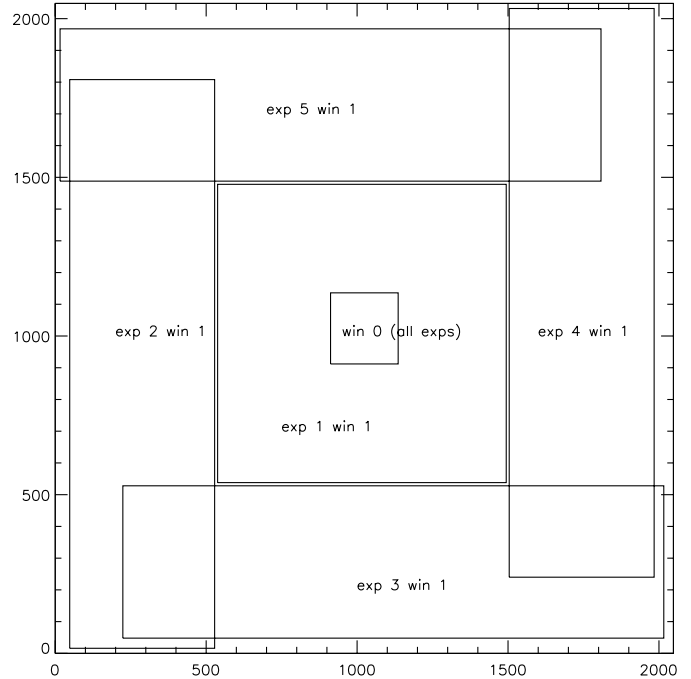


**Fig. 2.** Setup of XMM-OM imaging default mode. There are 5 exposures, each one being made up of two image mode windows: win 0 and win 1. Win 0 is the same for each exposure and is unbinned (0.5 arcsec). Win 1 for each exposure is binned  $2 \times 2$  pixels and the position changes for each exposure. For exposure 1, win 1 is a square containing the central half of the FOV, with win 0 entirely inside it. For the other exposures, win 1 is arranged to fill in the rest of the FOV

direction of the spacecraft is corrected in the image by tracking guide stars (Sect. 5.5).

*Fast Mode* emphasizes timing information at the expense of spatial coverage. The maximum total number of pixels that can be specified for a Fast Mode window is 512. Thus the maximum size of an approximately square window would be  $22 \times 23$  pixels (= 506 total). Note that there is no binning within a Fast Mode window. The pixel locations of individual photons within the window are recorded and assigned a time tag, which has a user-specified integration time of between 100 ms and the tracking frame duration (10–20 s). No tracking correction is applied to Fast Mode data. This can be applied on the ground, from the drift history supplied by XMM-OM.

To simplify observation set-up, two standard observing sequences of five exposures have been created that together cover the whole XMM-OM FOV at one arcsec sampling while at the same time monitoring a central target at full spatial sampling (0.5 arcsec). In the first variant, each of the five exposures contains an unbinned Image Mode window centred on the prime instrument's boresight (the position of the main target), and a second Image Mode window, binned by  $2 \times 2$  pixels, that is defined in each of the set of five exposures so as to form a mosaic of the entire field (see Fig. 2). The second variant is exactly the same as the first except that a Fast Mode window is added around the prime instrument's boresight position.

**Table 1.** OM filters, with the  $V$ -magnitude brightness limits for the main optical and UV filters, for a range of stellar types, assuming that they are not in the centre of the FOV. (Note the order of the filter elements in this table is not the order in which they should be used; see Table 2)

	B0	A0	F0	G0	K0	M0
$V$	7.71	7.68	7.65	7.65	7.63	7.59
$B$	9.38	9.18	8.83	8.58	8.29	7.68
$U$	9.79	8.34	7.88	7.57	6.66	4.50
UVW1	9.49	7.55	6.53	5.98	3.89	1.50
UVM2	8.94	6.82	4.53	2.70	-0.23	-2.63
UVW2	8.76	6.55	3.83	1.86	-0.63	-1.80
Mag	10.03	9.68	9.41	9.27	9.13	8.91
White	11.58	10.28	9.72	9.50	9.22	8.93

The length of an XMM-OM Image Mode only exposure can be set in the range 800–5000 s. However it should be noted that there is an approximately 300 s overhead associated with each individual exposure. The maximum length of an exposure that contains a single Fast Mode window is 4400 s, or 2200 s if there are two Fast Mode windows.

At the time of writing a further mode is being commissioned which allows the full field to be imaged at 1 arcsec sampling in one go, at the expense of tracking information and correction. This is made possible by the impressive stability of the *XMM-Newton* spacecraft compared to pre-launch expectation.

Window coordinates can be specified either in detector pixels, or in sky coordinates. To facilitate the latter, the XMM-OM performs a short  $V$ -band observation at the start of each pointing. The DPU compares the image with the positions of uploaded field stars to calibrate the absolute pointing of the OM.

### 3.2. Filter selection

The XMM-OM filter wheel rotates in one direction only and, to conserve the total number of wheel rotations over the expected lifetime of *XMM-Newton*, the number of filter wheel rotations per pointing is limited to one (unless there are very strong scientific arguments for more). Thus filter observations have to be executed in a particular order during a given target pointing. The filter elements are listed in the order they occur in the filter wheel in Table 2. The instrument is slewed with the blocked filter in place, and thereafter a field acquisition exposure is performed in  $V$ .

The same telescope focus setting is used for all the filters except for the Magnifier (see Sect. 5.6.1), where the optimum focus is different (the image quality is the most sensitive to focus position when using the Magnifier).

The XMM-OM instrument is optimised for the detection of faint sources. If the source count-rate is too high the response of the detector is non-linear. This “coincidence loss” occurs when the probability of more than one photon splash being detected on a given CCD pixel within the same CCD readout frame becomes

significant. Coincidence loss is discussed in more detail in Sect. 5.2. If a source is predicted to exceed the coincidence threshold for a given filter, then a different filter with lower throughput can be selected. Alternatively a grism can be selected which disperses the available light over many pixels.

The XMM-OM detectors can also be permanently damaged by exposure to a source that is too bright, reducing both the quantum efficiency of the photocathode and the gain of the channelplates. This is a cumulative effect dependent on the total number of photons seen over the lifetime of the instrument at a particular location on the detector. The deterioration is therefore more severe for longer observations of a bright source. For this reason limits are imposed on the maximum brightness of stars in the FOV (see Table 1) and apply to any star in the FOV irrespective of whether it is within a science window or not. Even more stringent limits are applied to the central region of the detector that will usually contain the target of interest. In the event that there is a star in (or near to) the FOV that violates the brightness constraints, a different filter, which has lower photon throughput, can be selected. Also, if the bandpass is appropriate, the Magnifier can be used to exclude bright stars further than a few arcmin from the field centre.

The grisms (one optimised for the UV, the other for the optical) form a dispersed first order image on the detector, together with a zeroth order image that is displaced in the dispersion direction. The counts in the zeroth order image of field stars determines the brightness limits used for observing with the grisms.

## 4. OM performance

The first light observation for XMM-OM took place on 2000 January 11. Since then the various engineering and science data taking modes of the instrument have been commissioned including full-field image engineering mode (not generally available for science observations because of the very large telemetry overhead required to transmit the data to the ground), and the Image and Fast science modes. The telescope focus has been optimised using the heater-based fine focus control, and the gain of the image intensifier has been optimised. The performance of the DPU in tracking image motion due to spacecraft drift has also been verified and distortion maps derived to relate XMM-OM detector coordinates to the sky. Photometric calibrations have been derived for all filter elements, but work continues on colour equations and to tie these more accurately into standard systems. Similarly, preliminary throughput and wavelength calibrations have been derived for the Grisms.

To illustrate the capabilities of XMM-OM, we show in Fig. 3 images of part of the Lockman Hole field in the White Light filter, and in five of the six colour filters (the remaining filter, UVM2, was not used during this observation). The images contains an  $R = 18.1$  mag AGN identified in the ROSAT observation of the field, and referred

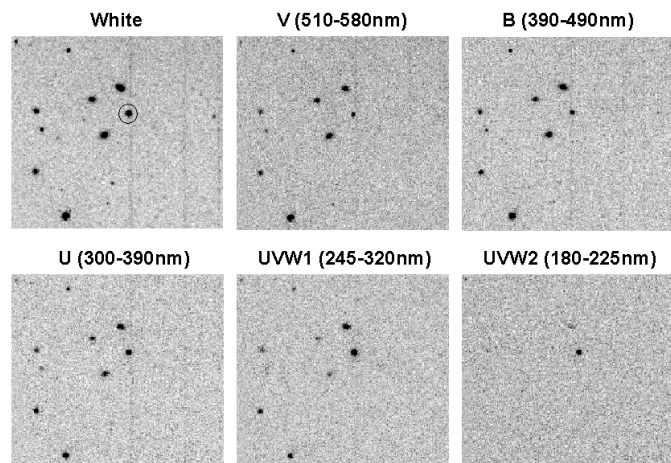


**Fig. 3.** An image of part of the Lockman Hole field taken in various XMM-OM filters as marked. The object circled in the White Light image is an AGN, referred to as R32 by Schmidt et al. (1998). The size of the images is about 3.5 arcmin across and the exposure times were 1500 s (white), 1000 s (*V*), 1000 s (*B*), 1000 s (*U*), 2200 s (UVW1) & 4400 s (UVW2). Faint vertical bars in some of the images are caused by charge leakage along the readout direction of the CCD from bright stars outside the illustrated field

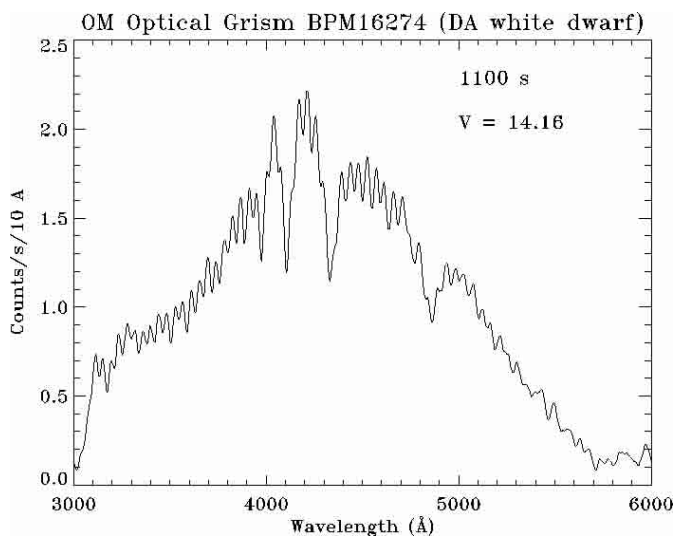


**Fig. 4.** Spectrum of the white dwarf BPM16274 obtained using the visual grism. The regular low-level fluctuations in the signal with wavelength are due to the modulo-8 pattern (Sect. 5.6.3), which has not been corrected in this plot

to as R32 by Schmidt et al. (1998). The AGN is clearly UV bright. The XMM-OM detects approximately  $12 \text{ count s}^{-1}$  from the AGN in White Light, while the count rate in the colour filters ranges from a high of  $2.9 \text{ count s}^{-1}$  in *U*, down to about  $0.25 \text{ count s}^{-1}$  in the UV filter UVW2.

To illustrate the spectral capability of XMM-OM, we show in Fig. 4 the extracted spectrum of the DA white dwarf standard BPM16274. The Balmer absorption lines can be clearly discerned.

**Table 2.** The OM filters, their wavelength bands in nm, and the preliminary zero points. The zero points will be updated once the data of the ground based observation programme become available in October 2000. The filters are in the order they occur in the filter wheel

Filter	wavelength band (nm)	zeropoints (mag)
Blocked		
<i>V</i>	510–580	18.11
Magnifier	380–650	
<i>U</i>	300–390	18.24
<i>B</i>	390–490	19.28
White (clear)	150–500	
Grism 2 (vis)	290–500	
UVW1	245–320	17.37
UVM2	205–245	16.02
UVW2	180–225	15.17
Grism 1 (UV)	200–350	

## 5. Analysis issues

### 5.1. Throughput

An initial estimate of the zero points of the various XMM-OM broadband filters (i.e. the magnitude which yields 1 count per second; Table 2) was derived from calibration observations of two white dwarfs.

- The OM response throughput was determined based on measurements of the spectrophotometric standards BPM16274 and LBB227;
- Using the OM throughput model an OM exposure of Vega was simulated;
- The zeropoints in *U*-, *B*-, *V*-filter were fixed in a way that the brightness of Vega matches the literature values;
- In the UV-filters the brightness of Vega was set to 0.025 mag; the average *U* magnitude of Vega in the literature being the most appropriate for the UV filters, and to 0.03 mag (the average Vega *V* magnitude) for the broadband Magnifier and the White Light filters.

The calculated OM zeropoints are written into the relevant XMM-CCF file, to be used by the XMM Science Analysis System (SAS) (Watson et al. 2001). Updates of the zeropoint definitions as well as more precise colour transformations (Royer et al. 2000) to the standard *UBV* system are expected once the results of a dedicated ground based photometric observation programme become available. In the framework of this programme several OM calibration fields are anchored to high quality secondary photometric standards deep fields established by ESO. Early results of this ground observations are expected in October 2000.

From analysis of the Lockman Hole field, avoiding the central 1 arcmin of the FOV where the background is enhanced (Sect. 5.6.4) the limiting magnitude after 1000 s is calculated to be 21.0 in *V*, 22.0 in *B* and 21.5 in *U* (6 sigma). The limiting magnitude for the White Light

filter is very dependant on the spectral type of the star, because the bandpass is so broad. However, for an A0 star we estimate that the 6 sigma limiting magnitude above background is  $\sim 23.5$ .

### 5.2. Coincidence loss and deadtime

Coincidence loss is observed whenever the count rate is such that more than one photon arrives in the same place within a given readout frame. Losses become significant for a point source at a count rate of about 10 count  $s^{-1}$  (for 10% coincidence) when the full CCD chip is being readout (i.e. about 2.5 magnitudes brighter than the zero points listed in Table 2). A factor of approximately two improvement can be achieved by restricting the area of the CCD used, since this reduces the time required to readout the chip.

The coincidence loss can be approximated by

$$ph_{in} = \frac{\log(1 - cts_{detected} T)}{T_{ft} - T} \quad (1)$$

where	
$ph_{in}$	infalling photon rate per second
$cts_{detected}$	measured count rate per second
$T$	CCD frametime in units of seconds
$T_{ft}$	frametransfer time in units of seconds.

Equation (1) applies strictly in the case of a perfectly point-like source. In practice a real stellar profile has wings, and the formula will break down at very high rates when coincidence among photons in the wings of the profile becomes significant.

The CCD deadtime depends on the size and shape of the science window used but can be calculated accurately. The deadtime correction should be applied by the SAS after any coincidence loss corrections.

### 5.3. Flat fields

An LED can be used to illuminate the detector by backscatter of the photons from the blocked filter. These images are not completely flat due to the illumination pattern of the LED, the gross shape of which could be removed by comparing with sky flats. However, using the LED allows a large number of events to be collected in every pixel to give sufficiently high statistics for pixel to pixel sensitivity to be measured and the relative measurement of any variation of the detector response on a fine scale. The LED brightness is adjustable and is currently operated at a level that produces  $3.25 \cdot 10^{-3}$  count  $s^{-1}$  per binned ( $2 \times 2$ ) pixel. So far, flat fields have been obtained to the level of 400 counts per binned ( $2 \times 2$ ) pixel allowing an accuracy of 5% in the sensitivity measurement. A CCF file in the SAS currently represents the accuracy of flat fields obtained before mid June, which is at the 10% level. Once sufficient flat fields have been obtained for a 2–3% sensitivity the relevant CCF file will be updated.

### 5.4. Background

The background count rate in the OM is dominated by the zodiacal light in the optical. In the far UV the intrinsic detector background becomes important. Images are regularly taken with the blocked filter and no LED illumination to measure the detector dark counts.

The mean OM dark count rate is  $2.56 \cdot 10^{-4}$  count  $s^{-1}$  per pixel. The variation in dark count rate across the detector is  $\pm 9\%$  and shows mainly a radial dependence, being highest in an annulus at about 8 arcmin radius and lowest in the centre. When the spacecraft is pointing at a very bright star, the dark rate is noticeably increased (e.g. up to 65% higher for the  $V = 0$  star Capella) despite the blocked filter. Excluding those dark frames taken during Capella ( $V = 0$ ) and Zeta Puppis ( $V = 2$ ) observations, the counts per dark frame vary by only  $\pm 7\%$  and show no trend of change with time.

### 5.5. Tracking performance

The positions of selected guide stars in the XMM-OM FOV are measured each 10–20 s tracking frame, and an X-Y offset applied to image mode data obtained during the tracking frame before they are added to the master image in the DPU memory. The tracking offsets are computed in pixels irrespective of the binning parameter chosen. Using this “Shift and Add” technique, the final image is corrected on timescales greater than a few tens of seconds and on spatial scales down to  $\sim 0.5$  pixels, for drift in the pointing direction of the spacecraft.

The performance of tracking can be verified by comparing the PSFs of stars taken during Fast Mode (at high time resolution and with no tracking) with those data taken using Image Mode when tracking is enabled. This analysis has shown that XMM-OM tracking is performing as expected.

Analysis of OM tracking histories show that the spacecraft drift is less than 0.5 pixels for approximately 75% of all frames taken, and therefore require no shift and add correction (a shift of one pixel will be made if the guide stars are calculated to have drifted more than  $\pm 0.5$  pixels from their reference positions). Of the remaining, the corrections due to drift are rarely more than 2 pixels in any one direction.

Tracking is turned off automatically when no suitable guide stars are found, which is usually due to poor statistics. This can occur in observations of very sparse fields (rare) or when using the UVM2 and UVW2 filters, where throughput is lower than in the optical bands. However, given the pointing stability of *XMM-Newton* and the intrinsically poorer resolution of the detector in the UV (Sect. 5.6), this does not normally lead to any significant degradation in the PSF for non-magnified data.

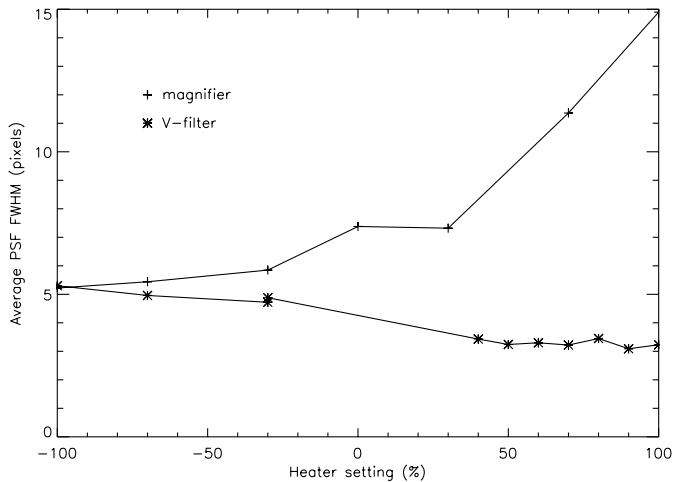


**Fig. 5.** PSF width with changing heater setting. Each point in the V-filter represents the average of 23 stars in the BPM16274 field

## 5.6. Image quality

### 5.6.1. Point Spread Function

After launch the measured PSFs in the V-filter had FWHM widths broader than expected from preflight measurements. The focus was therefore adjusted using the control heaters as discussed in Sect. 2.3. Figure 5 shows the gradual change in the PSF with the heater setting. As can be seen from the figure, the optimum setting for the Magnifier is clearly at  $-100\%$  i.e. at the minimum separation of the primary and secondary mirrors, whereas for the V-filter it is above  $70\%$ . A value of  $100\%$  (maximum separation of mirrors) was chosen for subsequent measurements in all filters, except for the Magnifier where  $-100\%$  is selected. To allow for the thermal settling time involved in a change of focus, twenty minutes of additional overhead time is inserted before and after a sequence of Magnifier exposures.

The PSFs contain a contribution from the telescope optics and from the detector. They can be assumed to be radially symmetric in shape, with an approximately gaussian central peak and extended wings. The width of the PSF increases with photon energy because of the detector component, from 3.1 pixels (1.5 arcsec) FWHM in the V band to  $\sim 6$  pixels (3 arcsec) pixels in the UV filters (see Fig. 6).

### 5.6.2. Distortion

The XMM-OM optics, filters and (primarily) the detector system result in a certain amount of image distortion. It is mainly in the form of barrel distortion, and if not corrected can result in shifts from the expected position of up to 20 arcsec. By comparing the expected position with the measured position for a large number of stars in the FOV a distortion map has been derived. The preliminary V-filter analysis was performed on the LMC pointing and is based on 230 sources. A 3rd order polynomial was

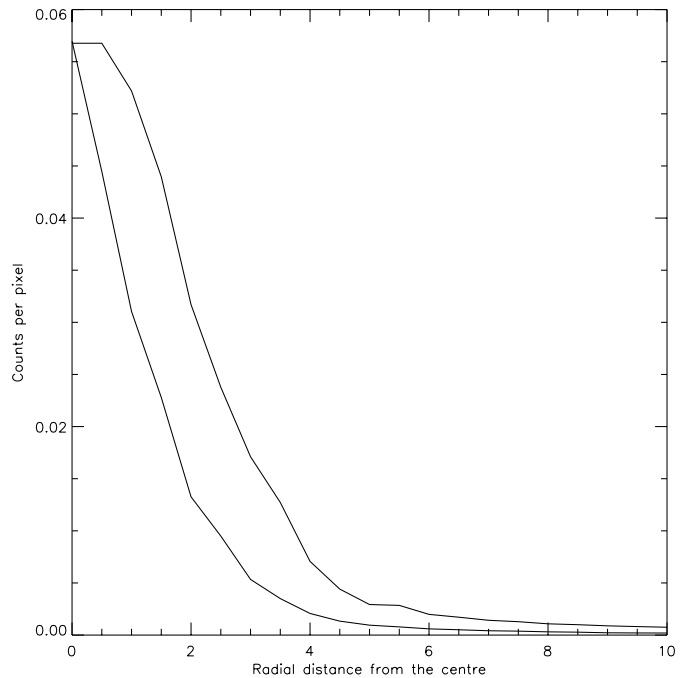


**Fig. 6.** Point spread function radial distribution. The inner curve is the average PSF of 23 stars from the V-filter; the outer curve from the UVW1-filter

fitted to the deviations assuming that there is no error at the centre of the FOV (i.e. at address (1024.5,1024.5)). This polynomial can be used to correct source positions measured in other fields, and currently gives a positional rms accuracy of 1.0 arcsec (1.9 pixels) in the V-filter (see Fig. 7; astrometry relative to stars of known position over restricted regions of the field can of course be more accurate than this). Using higher orders of the polynomial does not increase the accuracy and is detrimental particularly for sources at the edges of the FOV. Using functions other than polynomials has not yet been investigated, but may lead to an improvement to the correction for sources near the edges of the FOV. Distortion maps using the 3C 273 field have been derived for the other filters, but are not yet to such high accuracy. Further work will either use fields with more sources in the FOV or combine data from several observations. The preliminary distortion maps have been entered into the appropriate CCF files and can be used in conjunction with the SAS. They are also used on board to automatically position windows on the detector that are specified in sky coordinates. This is important for small windows such as those used in Fast Mode.

### 5.6.3. Modulo-8 pattern

As discussed earlier, the XMM-OM detector functions by centroiding a photon splash to within a fraction (1/8th) of a physical CCD pixel. This calculation is performed in real-time by the detector electronics, and therefore has to be fast. It is done by means of a lookup table whose parameters are computed onboard once per revolution, based on a short image taken with the internal flood LED

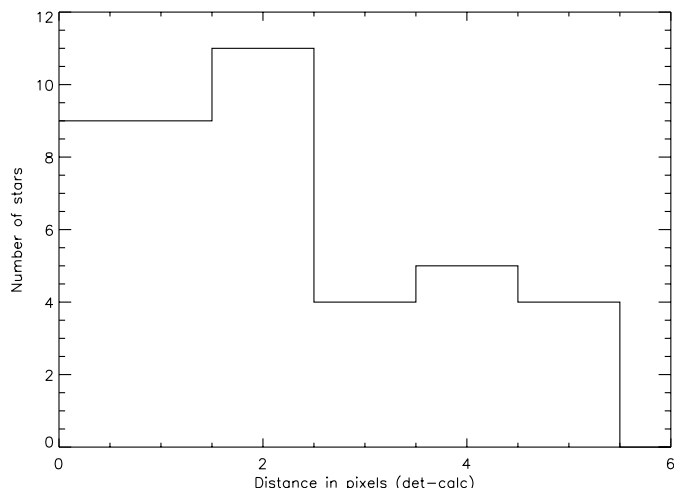


**Fig. 7.** Positional error of sources after the preliminary distortion correction. This histogram was made using sources from the 3C 273 field fitted to a map derived from the LMC field. The higher deviations occur near the edge of the FOV. The rms positional deviation is 1.9 pixels, equivalent to 1 arcsec

lamp, and periodically updated. The lookup table parameters are the mean values derived from a selected part of the active area of the detector (usually the central region). They do not take into account small variations in the shape of the photon splash over the detector face and as such are an approximation to the optimum value at a given location on the detector.

The result of imperfections in the lookup table is that the size of the pixels is not equal on the sky. When displayed with a normal image display routine, therefore, uncorrected XMM-OM images can exhibit a faint modulation in the apparent background level repeating every eight pixels, corresponding to every physical CCD pixel (see Fig. 8). SAS tasks that, for example, search for sources in XMM-OM images take the variation in pixel size into account and compute the local  $8 \times 8$  pattern post facto based on the measured image. Similarly the raw image can be resampled for display purposes. The SAS routine does not lose or gain counts, but resamples them according to the true pixel sizes.

The detector centroiding process also breaks down if more than one photon splash overlaps on a given CCD frame. Thus an  $8 \times 8$  pattern is often seen around bright stars (see Fig. 8a), or when two bright stars occur close together on an image.

#### 5.6.4. Scattered light

Artifacts can appear in XMM-OM images due to light being scattered within the detector. These have two causes: internal reflection of light within the detector window and reflection of off-axis starlight and background light from part of the detector housing.

The first of these causes a faint, out of focus ghost image of a bright star displaced in the radial direction

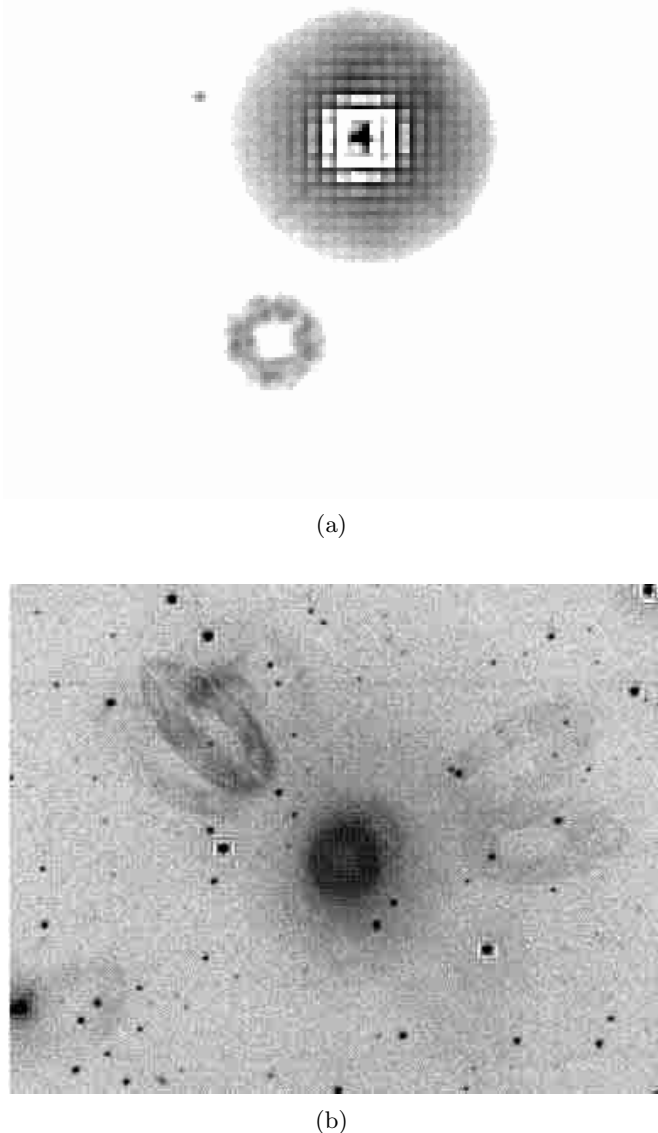


**Fig. 8.** The dynamic scale in these images has been chosen to enhance the straylight features. **a)** (*Top panel*): An out-of-focus ghost image of a bright star, taken from the 3C 273 field. This star has a photographic magnitude of 10.7. **b)** (*Bottom panel*): Straylight ellipses caused by reflection of a star outside the FOV, taken from PKS 0312 offset 6 field. The average background count rate is  $15 \text{ count pix}^{-1}$ ; in the bright straylight loop it is  $30 \text{ count pix}^{-1}$ . The background is also enhanced in the central region due to reflection of diffuse sky light from outside the field. In the centre it rises to  $\sim 3$  times the background, in the V band

away from the primary image due the curvature of the detector window (Fig. 8a).

The second effect is due to light reflecting off a chamfer in the detector window housing. Bright stars that happen to fall in a narrow annulus 12.1 to 13 arcmin off axis shine on the reflective ring and form extended loops of emission radiating from the centre of the detector (Fig. 8b). Similarly there is an enhanced “ring” of emission near



the centre of the detector due to diffuse background light falling on the ring (Fig. 8b).

The reflectivity of the ring, and of the detector window, reduces with increasing photon energy. Therefore these features are less prominent when using the UV filters.

## 6. Conclusion

The first stage of commissioning and calibrating XMM-OM has been completed. The instrument is fulfilling its role of extending the spectral coverage of *XMM-Newton* into the ultraviolet and optical band, allowing routine observations of targets simultaneously with EPIC and RGS. Specifically, the instrument has successfully been demonstrated to provide wide field simultaneous imaging with the X-ray camera, simultaneous timing studies, and bore-sight information to arcsec accuracy. A number of results illustrating the scientific potential of XMM-OM are contained within this volume.

*Acknowledgements.* We would like to thank all the people who have contributed to the instrument; in its building, testing and operation in orbit, as well as those who have analysed the calibration data. The author list only contains a small fraction of those people involved. XMM-OM was built by a consortium led by the Principal Investigator, Prof. K. O. Mason, and comprising, in the UK, the Mullard

Space Science Laboratory and Department of Physics and Astronomy, University College London; in the USA, University of California Santa Barbara, Los Alamos National Laboratory, & Sandia National Laboratory; and in Belgium, the Centre Spatial Liège & the University of Liège.

JMV acknowledges support from the SSTC-Belgium under contract P4/05 and by the PRODEX XMM-OM Project. The U.S. investigators acknowledge support from NASA contract NAS5-97119. The UK contribution was supported by the PPARC.

Based on observations obtained with *XMM-Newton*, an ESA science mission with instruments and contributions directly funded by ESA Member States and the USA (NASA).

## References

- Fordham, J. L. A., Bone, D. A., Norton, R. J., & Read, P. D. 1992, Proc. ESA Symp. on Photon Counting Detectors for Space Instrumentation, ESA SP-356, 103
- Jansen, F., Lumb, D., Altieri, B., et al. 2001, A&A, 365, L1
- Kawakami, H., Bone, D., Fordham, J. L. A., & Michel, R. 1994, Nucl. Instrum. Meth. A, 348, 707
- Royer, P., Manfroid, J., Gosset, E., & Vreux, J.-M. 2000, A&AS, 145, 351
- Schmidt, M., Hasinger, G., Gunn, J., et al. 1998, A&A, 329, 495-503
- Watson, M. G., Auguères, J.-L., Ballet, J., et al. 2001, A&A, 365, L51